Hindawi
International Journal of Aerospace Engineering
Volume 2023, Article ID 1282797, 9 pages
https://doi.org/10.1155/2023/1282797

Research Article

The Pretension Design of Cable Mesh considering the Large Deformation of Ring Truss

Hu Jianfeng, Wang Lipeng, and Yang Jungang

China Academy of Space Technology (Xi'an), Xi'an 710100, China

Correspondence should be addressed to Hu Jianfeng; 1271290515@qq.com

Received 8 December 2022; Revised 15 February 2023; Accepted 24 February 2023; Published 11 March 2023

Academic Editor: Zhiguang Song

The conventional pretension design of cable mesh usually takes the ring truss as a rigid body or assumes small deformation. This method needs to be more accurate in designing super large aperture antennas. A cable mesh design method considering the large deformation of the ring truss is proposed in this paper based on the flexible multibody dynamics (FMD) and the force density method (FDM). With this method, the significant range deviation of the boundary points' position of the ring truss under the tension of the external area of the cable mesh after the completion of the pretension design can be predicted with high accuracy. After the ring truss and cable mesh surface are assembled stably, there is only a minimal deviation between the actual mesh surface and the theoretical mesh surface of the antenna, and there is only a minimal deviation between the genuine mesh pretension and the design pretension. The above calculation method is verified by numerical simulation, and the simulation results show that the technique can be applied to the mesh pretension design of a super large aperture ring deployable antenna.

1. Introduction

With the development of electronic reconnaissance and mobile communications, the demand for a super large aperture antenna is increasingly urgent. The large ring deployable antenna has become one of the research hot spots in the world for its lightweight and high storage ratio [1, 2]. The deployable ring antenna mainly consists of a ring truss, front mesh, metal mesh, rear mesh, and tension ties, as shown in Figure 1(a). The ring truss is mainly composed of the quadrilateral element that consists of the longeron, batten, thick diagonal, thin diagonal, T-shaped connection, and synchronous connection, as shown in Figure 1(b). The rod is usually made of light and long composite thin-walled pipe fittings, and the connection is usually made of high-strength and high-rigidity metal. The connecting part between the cable mesh and the ring truss is called the external mesh area; the rest is called the internal mesh area. The mesh model pretension design is one of the key issues that researchers focus on during the development of the deployable ring antenna [3–5]. At present, the cable mesh pretension design methods of large deployment antennae include the force density method [6, 7], the equilibrium matrix method [8, 9], and the dynamic relaxation method [5]. In addition, in recent years, some scholars have assumed that the ring truss occurs small deformation and performed the cable mesh pretension design by using the overall calculation method of the ring antenna [10, 11]. The above methods usually assume that the ring truss is rigid or occurs small deformation in the design of mesh pretension. However, with the increased antenna aperture, the super large aperture ring truss always produces large deformation and displacement under the cable mesh tension. With the mesh pretension design method that assumes the ring truss is rigid or occurs small deformation for super large aperture ring antenna, if the mesh is connected to the deployable truss according to the theoretical design in the real assembly environment, the connection nodes for the mesh and ring truss are deviated from the initial design and the mesh pretension is reduced to a certain extent compared with the initial pretension. Therefore, the mesh surface accuracy and pretension cannot meet the initial design requirements. The larger the reflector aperture, the greater the difference, as shown in Figure 2.

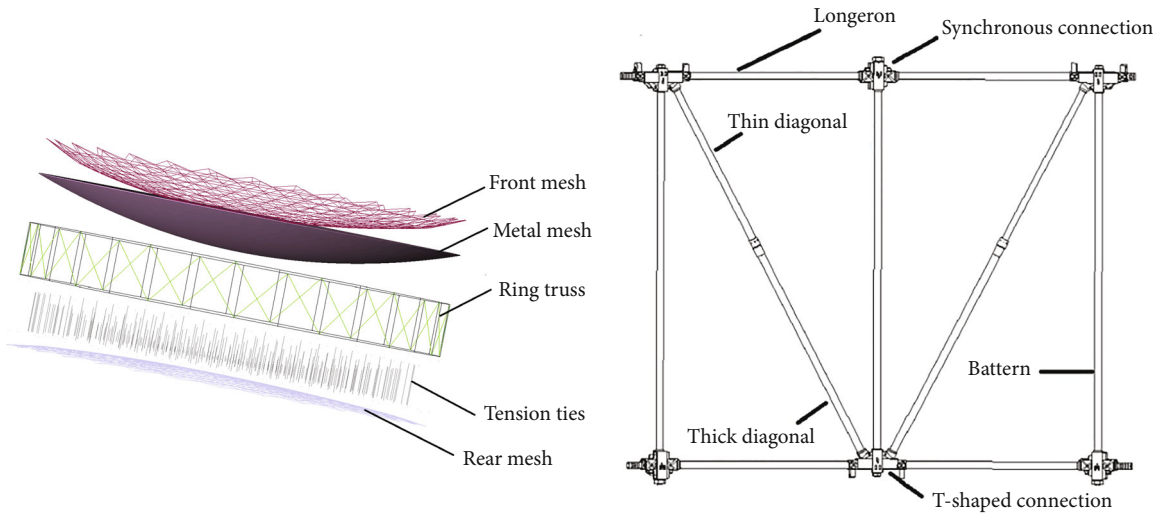

(a) Components of AstroMesh I antenna (b) Quadrilateral element

Figure 1: The composition of the ring deployable antenna.

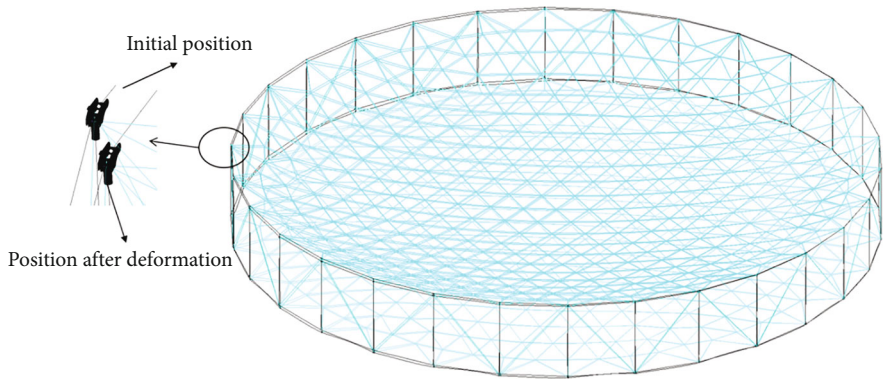

Figure 2: The deformation of the ring truss under the cable mesh tension.

In recent years, researchers from Tsinghua University and China Academy of Space Technology applied the flexible multibody system dynamic theory to the dynamic simulation of the deployment process and structural optimization design of large deployable antenna [12–17]. They precisely predicted the large deformation and displacement of flexible rods which cannot be completed by the traditional finite element method during the deployment process of a large deployable antenna in ground test and orbit environments, and the simulation is proved by ground tests and observation in space.

However, few literatures are found on the research of the mesh design for super large aperture antennas. For this purpose, this paper proposes a cable mesh pretension method that considers the large deformation of the ring truss based on the flexible multibody dynamic theory as mentioned above. This method takes the large displacement and deformation of the ring truss under the mesh pretension into full consideration. Therefore, the connection node for the ring truss and the cable mesh after deformation has a very minimal deviation from the theoretical design. In this way, the mesh pretension is almost consistent with the design pretension. Finally, the antenna has high mesh surface accuracy, and the actual mesh and design pretension meet the accuracy requirements. The simulation results show that this method is correct and effective and can be used for the cable mesh design of the deployable ring antenna with a super large aperture.

2. The Force Density Method

The force density method is basically to establish the force equilibrium equation of each node on the equilibrium geometries of the cable mesh structure and convert the nonlinear balance equation into a linear system of equations for the solution by introducing the force density [18, 19].

As shown in Figure 3, the force equilibrium equation of the node i in the direction x in the mesh structure equilibrium state is

$$\sum_{j \in U_i} \frac{T_{ij}}{L_{ij}} \left(x_i - x_j\right) = f_{ix}. \tag{1}$$

In Formula (1), U_i is a set of nodes connected to node i. ij is the element that connects node i and node j. T_{ij} is the

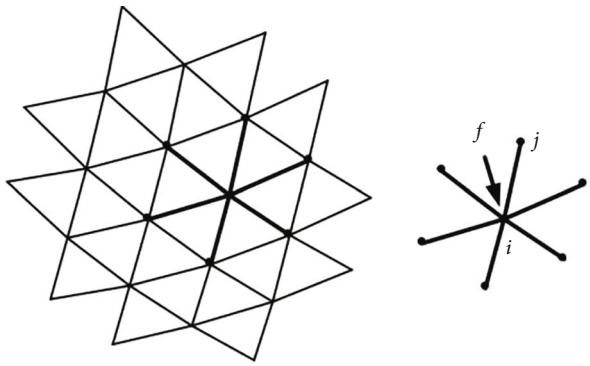

Figure 3: The force density method description.

tension of the element ij, and L_{ij} is the length of the element ij.

If $q_{ij} = T_{ij}/L_{ij}$ is defined as the force density of the element ij, the above formula can be expressed as

$$\sum_{j \in U_i} q_{ij}\left(x_i - x_j\right) = f_{ix}. \tag{2}$$

The force equilibrium equation for all nodes in the direction x in the mesh structure equilibrium state is written in the matrix form

$$\boldsymbol{C}^T \boldsymbol{Q} \boldsymbol{C} \boldsymbol{x} = \boldsymbol{f}_x, \tag{3}$$

where $\boldsymbol{C}$ is the structural topology matrix of $m \times n$, m is the total number of cable elements, n is the total number of nodes, and $\boldsymbol{Q}$ is a diagonal matrix of $m \times m$ consisting of the force density of cable elements. Suppose that in the n nodes, the number of free nodes is n_f, the number of fixed nodes is n_g, and the topological matrix $\boldsymbol{C}$ are divided into blocks $\boldsymbol{C}_f$ and $\boldsymbol{C}_g$. x_f is the coordinate of free nodes, x_g is the coordinate of fixed nodes, the external force on free nodes is equal to 0, and f_{xg} is the reaction force of fixed node support. Therefore, Formula (3) can be expressed as

$$\begin{pmatrix} \boldsymbol{C}_f \\ \boldsymbol{C}_g \end{pmatrix} \boldsymbol{Q} \left(\boldsymbol{C}_f \, \boldsymbol{C}_g\right) \begin{pmatrix} \boldsymbol{x}_f \\ \boldsymbol{x}_g \end{pmatrix} = \begin{pmatrix} \boldsymbol{0} \\ \boldsymbol{f}_{xg} \end{pmatrix}. \tag{4}$$

By solving Formula (4), the coordinates of all free nodes in the direction x and the force of fixed nodes in the direction x are obtained.

Similarly, the force equilibrium matrix of nodes y and z can be obtained. Thus, the coordinates of all free nodes and the fixed node forces are obtained. According to the obtained node coordinates, the length L_{ij} of the cable segment at the time of force balance can be calculated, and then, the cable force T_{ij} at the time of balance can be obtained by using $q_{ij} = T_{ij}/L_{ij}$. The pretension form finding for the ring deployable antenna is to ensure that by finding a set of force density, the coordinates of the free nodes of the cable mesh are at the theoretic coordinates when the cable mesh is balanced, and the cable mesh tension is as uniform as possible. In this paper, the objective optimization mathematical model is established with the cable segment force density as the design parameter. The optimization model is shown in Formula (5).

$$\begin{aligned} &\text{Find } q_1, q_2, \cdots q_m, \\ &\text{Min } f = \frac{T_{\max}}{T_{\min}}, \\ &\text{s.t.} \begin{cases} \boldsymbol{C}^T \boldsymbol{Q} \boldsymbol{C} \boldsymbol{x} = \boldsymbol{f}_x, \\ \boldsymbol{C}^T \boldsymbol{Q} \boldsymbol{C} \boldsymbol{y} = \boldsymbol{f}_y, \\ \boldsymbol{C}^T \boldsymbol{Q} \boldsymbol{C} \boldsymbol{z} = \boldsymbol{f}_z, \\ 0 < q_i < [q], i = 1 \sim m, \\ z_{fi} = \dfrac{x_{fi}^2 + y_{fi}^2}{4f}, \\ \left(x_{gi}, y_{gi}, z_{gi}\right)^T = \text{const}, \end{cases} \end{aligned} \tag{5}$$

where q_i is the force density of each segment, m is the number of segments for the cable structure, f is the objective function, $[q]$ is the maximum design allowable value of the force density of the cable segment, fi is the number of free nodes, and gi is the number of fixed nodes.

3. Dynamic Modelling of the Large Ring Truss

The deployable ring truss consists of the hinge with minimal deformation and the rod with large deformation. This paper assumes that the hinge is rigid, and its model is built based on the rigid body dynamics theory. The rod model is based on the geometrically exact beam theory [20, 21]. Finally, the constraints model is built based on the multirigid-body dynamic theory.

In the study of the flexible multibody dynamics, Lagrange's equation of first kind is adopted as the governing equation of the system dynamics as shown in Formula (6)

$$\begin{aligned} &\frac{d}{dt}\left(\frac{\partial T}{\partial \dot{\boldsymbol{q}}}\right) - \frac{\partial T}{\partial \boldsymbol{q}} + \frac{\partial V}{\partial \boldsymbol{q}} + \boldsymbol{\Phi}_{\boldsymbol{q}}^T \boldsymbol{\lambda} = \boldsymbol{Q}, \\ &\boldsymbol{\Phi}(\boldsymbol{q}, t) = \boldsymbol{0}, \end{aligned} \tag{6}$$

where T is kinetic energy, $\boldsymbol{q}$ is generalized coordinate, $\dot{\boldsymbol{q}}$ is generalized speed, V is elastic potential energy, $\boldsymbol{\Phi}$ is constraint equations, λ is the Lagrange multiplier, and $\boldsymbol{Q}$ is the generalized external force.

3.1. Rigid Body Modelling. The motion of a rigid body in three-dimensional space can be divided into the translation in three directions and the rotation in three directions. Each rigid body has 6-degree of freedom. In selecting generalized coordinates, the position of the center of mass of the rigid body is used to determine the translational configuration, there are many descriptions of rotation in literature [22]. In this paper, the rotation vector method is used to describe

the rotation of a rigid body. According to Euler's rotation theorem and the definition of the rotation vector [22], the rotation vector $\boldsymbol{\varphi}$ is parallel to the rotation axis $\boldsymbol{a}$, and the modulus is equal to the rotation angle. The conversion relationship from rotation vector $\boldsymbol{\varphi}$ to rotation matrix $\boldsymbol{A}$ is

$$\boldsymbol{A} = \boldsymbol{I} + h_1\tilde{\boldsymbol{\varphi}} + h_2\tilde{\boldsymbol{\varphi}}\tilde{\boldsymbol{\varphi}}, \tag{7}$$

where $\boldsymbol{I}$ is the 3D identity matrix and h_1 and h_2 are the functions of the rotation angle φ

$$h_1 = \frac{\sin\varphi}{\varphi}, h_2 = \frac{1-\cos\varphi}{\varphi^2}. \tag{8}$$

$\tilde{\boldsymbol{\varphi}}$ is the antisymmetric matrix of the rotation vector $\boldsymbol{\varphi}$, and the three Cartesian components φ_1, φ_2, and φ_3 using $\boldsymbol{\varphi}$ can be expressed as

$$\tilde{\boldsymbol{\varphi}} = \begin{bmatrix} 0 & -\varphi_3 & \varphi_2 \\ \varphi_3 & 0 & -\varphi_1 \\ -\varphi_2 & \varphi_1 & 0 \end{bmatrix}. \tag{9}$$

The component form $\boldsymbol{\omega}$ and the rotation vector $\dot{\boldsymbol{\varphi}}$ of the angular velocity of the local coordinate system in the global coordinate system satisfy the following conversions to the time derivative:

$$\begin{aligned} \boldsymbol{\omega} &= \boldsymbol{H}(\boldsymbol{\varphi})\dot{\boldsymbol{\varphi}}, \\ \boldsymbol{H} &= h_1\boldsymbol{I} - h_2\tilde{\varphi} + h_3\varphi\varphi^T, \end{aligned} \tag{10}$$

where

$$h_3 = \frac{\varphi - \sin\varphi}{\varphi^3}. \tag{11}$$

In addition, the component form $\bar{\boldsymbol{\omega}}$ of the angular velocity of the rotation system of coordinates in the local coordinate system can be obtained by $\boldsymbol{\omega}$ multiplying the inverse matrix of $\boldsymbol{A}$

$$\bar{\boldsymbol{\omega}} = \boldsymbol{A}^T\boldsymbol{\omega} = \boldsymbol{A}^T\boldsymbol{H}\dot{\boldsymbol{\varphi}}. \tag{12}$$

It can be further proved that

$$\boldsymbol{H}^T = \boldsymbol{A}^T\boldsymbol{H}. \tag{13}$$

Finally, we can get

$$\bar{\boldsymbol{\omega}} = \boldsymbol{H}^T\dot{\boldsymbol{\varphi}}. \tag{14}$$

Considering that the rigid body has no elastic potential energy term, Formula (6) can be simplified as

$$\begin{aligned} \frac{d}{dt}\left(\frac{\partial T}{\partial \dot{\boldsymbol{q}}}\right)^T + \boldsymbol{\Phi}_q^T\boldsymbol{\lambda} &= \boldsymbol{Q}, \\ \boldsymbol{\Phi}(\boldsymbol{q}, t) &= \boldsymbol{0}, \end{aligned} \tag{15}$$

where $\boldsymbol{q} = [\boldsymbol{r}_i\ \boldsymbol{\varphi}_i]$ .The kinetic energy expression in the above formula is

$$T = \frac{1}{2}m_i\dot{\boldsymbol{r}}_i{}^T\dot{\boldsymbol{r}}_i + \frac{1}{2}\bar{\boldsymbol{\omega}}_i{}^T J_i\bar{\boldsymbol{\omega}}_i, \tag{16}$$

where J is the moment of inertia in the center of mass coordinate system.

3.2. Flexible Body Modelling. Under the external mesh cable tension, the composite thin-walled pipe fittings of the ring truss will have large-scale displacement and large deformation. According to the geometrically exact beam theory, the section curvature of any beam element with large deformation and large-scale rotation is geometrically accurate. Therefore, the model of the composite thin-walled rods using the geometrically exact beam theory is more accurate than the conventional finite element method. This paper uses the flexible beam model based on the geometrically exact beam theory. In the modeling process, the centerline position $\boldsymbol{r}$ at the left and right ends of the beam element and the rotation vector $\boldsymbol{\varphi}$ is selected as the generalized coordinates to describe the beam element configuration, as shown in Figure 4.

The generalized coordinates of the beam element can be expressed as

$$\boldsymbol{q}_b = \left[\boldsymbol{r}_1^T\ \boldsymbol{\varphi}_1^T\ \boldsymbol{r}_2^T\ \boldsymbol{\varphi}_2^T\right]^T. \tag{17}$$

For the interpolation of the rotation vector $\boldsymbol{\varphi}$, Crisfield and Jelenić [23] proposed to establish a reference coordinate system in the beam element and interpolate the rotation vector under the reference coordinate system. Without the influence of the reference coordinate system, the curvature obtained based on this calculation can be the same in any observation coordinate system. In this paper, the rotation vector is interpolated according to this method. The rotation vector of any node relative to the reference coordinate system is written as $\boldsymbol{\varphi}^r$. According to the above, any node of the centerline in the beam element $\boldsymbol{r}$ and $\boldsymbol{\varphi}^r$ are expressed as follows:

$$\begin{aligned} \boldsymbol{r} &= (1-\xi)\boldsymbol{r}_1 + \xi\boldsymbol{r}_2, \\ \boldsymbol{\varphi}^r &= (1-\xi)\boldsymbol{\varphi}_1^r + \xi\boldsymbol{\varphi}_2^r, \end{aligned} \tag{18}$$

where $\xi \in [0, 1]$ is the parameter coordinates in the beam element. According to the above beam element functions, it can be expressed as follows:

$$T_b = \frac{L}{2}\int_0^1 \rho A\dot{\boldsymbol{r}}^T\dot{\boldsymbol{r}} + \bar{\boldsymbol{\omega}}^T J\bar{\boldsymbol{\omega}}\big]\,d\xi, \tag{19}$$

where L is the length of the beam element and A is the cross-section area of the element.

The beam element's potential energy can be expressed as

$$V = \frac{L}{2}\int_0^1 \left[\boldsymbol{N}^T(\boldsymbol{\gamma} - \boldsymbol{\gamma}_0) + \boldsymbol{M}^T(\boldsymbol{\kappa} - \boldsymbol{\kappa}_0)\right]d\xi, \tag{20}$$

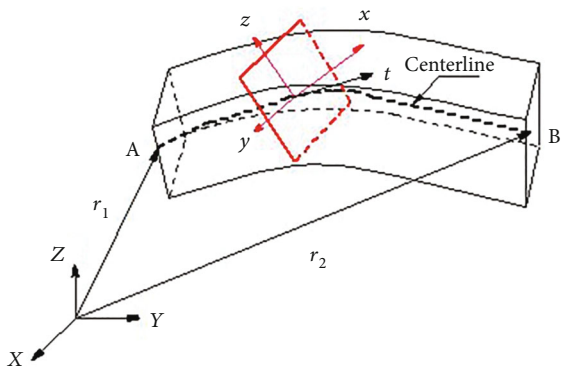

Figure 4: Flexible beam element.

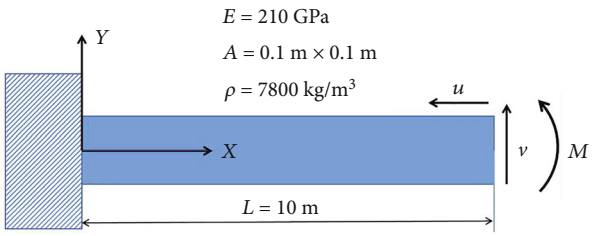

Figure 5: Cantilever beam undergoes bending load.

where

$$\begin{aligned} \boldsymbol{\gamma} &= \boldsymbol{A}^T \boldsymbol{r}', \\ \boldsymbol{\kappa} &= \boldsymbol{H}^T \boldsymbol{\varphi}', \\ \boldsymbol{N} &= \boldsymbol{C}_N(\boldsymbol{\gamma} - \boldsymbol{\gamma}_0), \\ \boldsymbol{M} &= \boldsymbol{C}_M(\boldsymbol{\kappa} - \boldsymbol{\kappa}_0), \end{aligned} \tag{21}$$

where $\boldsymbol{\gamma}$ is the strain vector, $\boldsymbol{\gamma}_0$ is the initial strain vector, $\boldsymbol{\kappa}$ is the curvature vector, $\boldsymbol{\kappa}_0$ is the initial curvature vector, and $\boldsymbol{N}$ and $\boldsymbol{M}$ are section force and moment, respectively. The above physical quantities can be expressed using the generalized coordinates. $\boldsymbol{C}_N$ and $\boldsymbol{C}_M$ are the constitutive matrix only related to the material and the section features.

3.3. Constraint Modelling. In the deployed state, the deployable ring antenna features a fixed constraint between the hinge and the batten, a fixed constraint between the thick diagonal and thin diagonal, and a rotational constraint between the thin diagonal and the hinge.

The beam section can be regarded as the rigid body according to the geometrically exact beam theory. Therefore, the constraint model can be processed as follows. Assuming a mark point on a beam section, the position and attitude of the mark point relative to the section center point will not change during the movement. Assuming that the coordinate system described by the attitude of the center point of the section is the rigid body coordinate system, record the relative position of the initial mark point in the coordinates system of the rigid body as $\boldsymbol{r}_m$. The component forms of this point in the coordinates system of the rigid body are recorded as $\boldsymbol{x}_m$, $\boldsymbol{y}_m$, and $\boldsymbol{z}_m$. If the position of the section center point in the global coordinate system is $\boldsymbol{r}$, the rotation vector is ϕ, and the vector rotation matrix is $\boldsymbol{A}$, the position $\boldsymbol{R}_m$ of the mark point in the global coordinate system is

$$\boldsymbol{R}_m = \boldsymbol{r} + \boldsymbol{A}\boldsymbol{r}_m. \tag{22}$$

In addition, the axial components $\boldsymbol{x}_m$, $\boldsymbol{y}_m$, and $\boldsymbol{z}_m$ of the mark point in the rigid body coordinate system and the components $\boldsymbol{X}_m$, $\boldsymbol{Y}_m$, and $\boldsymbol{Z}_m$ in the global coordinate system are, respectively,

$$\begin{aligned} \boldsymbol{X}_m &= \boldsymbol{A}\boldsymbol{x}_m, \\ \boldsymbol{Y}_m &= \boldsymbol{A}\boldsymbol{y}_m, \\ \boldsymbol{Z}_m &= \boldsymbol{A}\boldsymbol{z}_m. \end{aligned} \tag{23}$$

Table 1: Comparison of tip axial displacement using FDM and Ansys (m).

$ML/(\pi EI)$	Analytical	FDM	Ansys
0.2	0.64511	0.63937	0.64519
0.4	2.43173	2.40926	2.43191
0.6	4.95449	4.85451	4.44831
0.8	7.66128	7.56397	Unconverged
1	10.00000	9.96377	Unconverged

Table 2: Comparison of tip vertical displacement using FDM and Ansys (m).

$ML/(\pi EI)$	Analytical	FDM	Ansys
0.2	3.03958	3.01894	3.03971
0.4	5.49866	5.47749	5.49880
0.6	6.94455	6.97115	6.67273
0.8	7.19785	7.30276	Unconverged
1	6.36620	6.54480	Unconverged

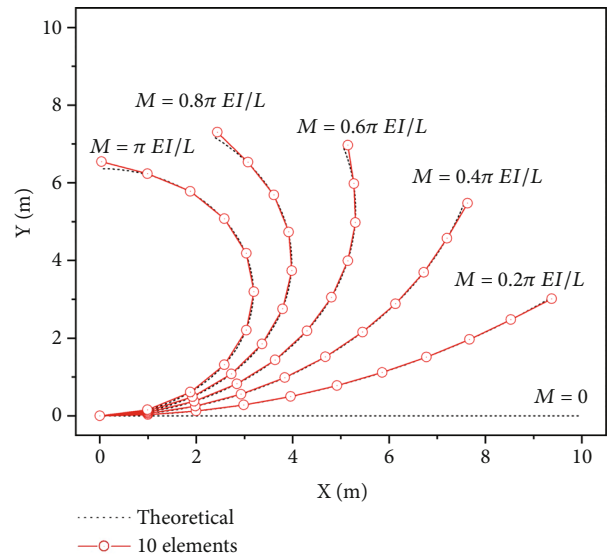

Figure 6: Large deformation of the cantilever under bending moments.

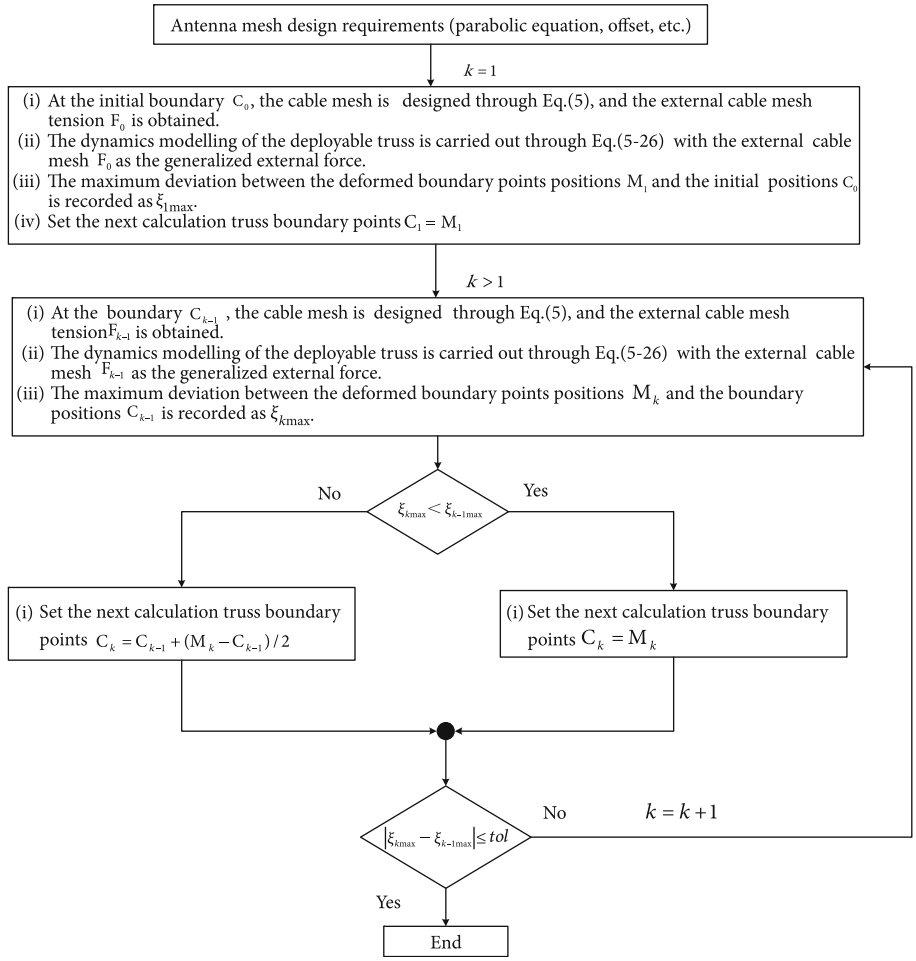

Figure 7: Antenna cable mesh design process.

Assume that the mark points of two different components forming a fixed constraint are, respectively, i and j. The fixed constraint requires that the position and altitude of two-mark points coincide completely and include 6 constraint equations.

$$\begin{aligned} &\boldsymbol{R}_{im} - \boldsymbol{R}_{jm} = \boldsymbol{0}, \boldsymbol{X}_{im} \cdot \boldsymbol{Z}_{jm} = 0, \\ &\boldsymbol{X}_{im} \cdot \boldsymbol{Y}_{jm} = 0, \boldsymbol{Y}_{im} \cdot \boldsymbol{Z}_{jm} = 0. \end{aligned} \tag{24}$$

Similarly, assume that two-mark points of two different components forming the revolute constraint are i and j. The revolute constraint requires that the positions of two-mark points coincide completely, and one of the coordinate systems coincides completely. The rotation around this axis is allowed between two-mark points. Assuming the rotation is around the z-axis, it contains five constraint equations.

$$\boldsymbol{R}_{im} - \boldsymbol{R}_{jm} = \boldsymbol{0}, \boldsymbol{X}_{im} \cdot \boldsymbol{Y}_{jm} = 0, \boldsymbol{X}_{im} \cdot \boldsymbol{Z}_{jm} = 0. \tag{25}$$

3.4. Large Deformation Numerical Example. A classical large deformation flexible beam test example [21, 24–26] (shown in Figure 5) is carried out to prove the availability of the proposed method in large deformation simulation calculation, and the test results are compared with the calculation results of commercial software Ansys Workbench 2020. There is an analytical solution for the concentrated bending moment of this cantilever beam; therefore, it is widely used in the test of large deformation beam modeling method.

Table 3: The parameters of simulation model.

Item	Calculation parameters
Antenna aperture	26 m
Antenna focal length	4 m
Rod inner diameter	22 mm
Rod outer diameter	24 mm
Rod elastic modulus	160 GPa
Cable diameter	5 mm
Cable elastic modulus	50 GPa
The average tension of front mesh	70 N
The average tension of rear mesh	180 N

The structural parameters of the cantilever beam are shown in Figure 5. During the calculation, the cantilever beam is divided by 10 elements. The proposed method integral error is set to $1e-3$ in this paper. The beam element is modelled by Beam188, and the convergence

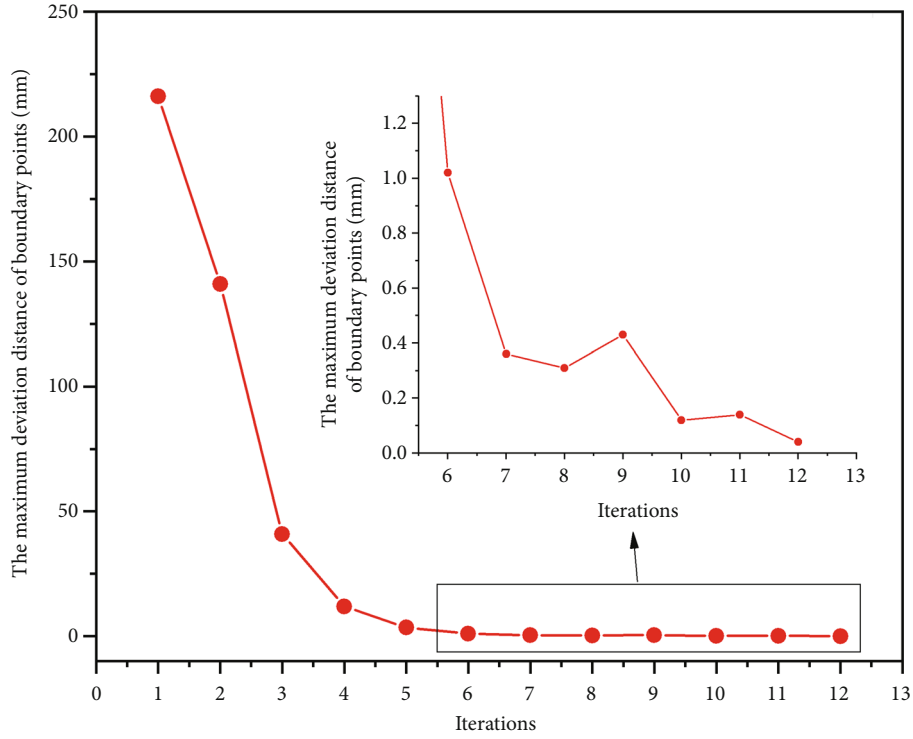

Figure 8: The change of the maximum deviation distance of boundary points with iterations.

criterion is carried out according to the system default criterion in Ansys.

According the test results shown in Tables 1 and 2 and Figure 6,when the applied torque does not exceed $(0.4\pi EI)/L$, the difference between the calculation of 10 elements using the proposed method and the theoretical value is within 1%, while Ansys has an error within 0.01%. When the applied torque is not lower than $(0.6\pi EI)/L$, Ansys has a larger error and its calculation even cannot converge. However, the proposed method still has high calculation accuracy, with the maximum within 2.8%.

The error can be further reduced to 0.05% by dividing into 50 elements with the proposed method. Even if Ansys increases the step size by 100 times and dividing into 100 elements, its calculation results cannot converge when calculating the applied torque $M = (\pi EI)/L$.

By comprehensive consideration, the proposed modeling method has more advantages than Ansys when dealing with the large deformation flexible beam element model.

4. The Cable Mesh Design Process

The cable mesh design process is shown in Figure 7. Firstly, at the initial theoretic boundary $\boldsymbol{C}_0$ of the truss, the initial mesh model is built using FDM and the mesh tension is optimized to be uniform. Then, the first set of mesh coordinates and the mesh element tension is obtained. The force $\boldsymbol{F}_0$ of the external mesh cable to the deployable truss at the connection between the cable mesh and the deployable truss is obtained. The large deformation rod model is built based on the geometrically exact beam theory. The minimal deformation hinge model and the constraint model are built based on the multirigid-body dynamic theory, thus achieving the dynamic modelling of the deployable truss. Considering that the cable mesh is connected to the deployable truss through the external mesh cable, the force $\boldsymbol{F}_0$ of the external mesh cable is applied to the deployable truss. The coordinates $\boldsymbol{C}_1$ of the deployable truss boundary after the deformation under the action $\boldsymbol{F}_0$ of the external mesh cable are obtained, and the displacement variation of each point $\boldsymbol{\xi}_1$ and the maximum displacement variation $\xi_{1\ \max}$ are calculated.

When the calculation time $k > 1$, only taking the new truss boundary $\boldsymbol{C}_{k-1}$ instead of the initial one and ensuring the others are unchanged (Formula (5)), a set of new mesh coordinates and the mesh element tension are obtained and the force $\boldsymbol{F}_{k-1}$ of the external mesh cable to the deployable truss at the connection between the mesh and the deployable truss is extracted.

The newly obtained external mesh cable tension $\boldsymbol{F}_{k-1}$ is applied to the deployable truss to obtain the coordinates $\boldsymbol{M}_k$ of the truss boundary after deformation. The displacement variation $\boldsymbol{\xi}_k$ of each node from the previous and the maximum displacement variation $\xi_{k\ \max}$ are calculated.

When $\xi_{k\ \max} < \xi_{k-1\ \max}$, set the next calculation truss boundary $\boldsymbol{C}_k = \boldsymbol{M}_k$ or set $\boldsymbol{C}_k = \boldsymbol{C}_{k-1} + (\boldsymbol{M}_k - \boldsymbol{C}_{k-1})/2$.

The difference between the relative distances of the truss boundary for the k time and for the $k-1$ time should be less than the allowable error, that is $|\xi_{k\ \max} - \xi_{k-1\ \max}| \le tol$. The error size is related to the mesh surface accuracy and the mesh tension uniformity. If the above requirement is not satisfied, continue to perform step (3); otherwise, stop the

calculation. The mesh is connected to the deployable truss without apparent position deviation or tension change due to truss deformation. The internal node coordinates and the mesh tension meet the theoretical design.

5. Simulation Example

The calculation program for the cable mesh design can be obtained through the numerical simulation and programming of the above cable mesh design method. In addition, the pretension design of a positive-feed ring deployable antenna with a 26 m aperture is performed in this paper. The primary antenna parameters are shown in Table 3.

Multiple iterative calculations are carried out through the above cable mesh design method. It can be seen from Figure 8 that in the early stage of iteration, the maximum displacement change before and after the boundary point deformation decreases rapidly. At the end of the iteration, the change is slow. After 13 counts, the maximum deviation of front and rear boundary points is less than 0.1 mm. When the maximum deviation is less than 0.1 mm, the cable mesh model is built based on the geometrically exact beam theory and the previous modeling method for the ring truss. After the cable mesh system is stable, the RMS deviation of the mesh surface accuracy from the theoretical form is only 0.006 mm, and the change of the cable mesh pretension is less than 0.5% of the initial design.

6. Discussion

At present, the pretension design process of large deployable ring antenna cable mesh is based on the assumption of rigidity or small deformation of the ring truss. However, large displacement and large deformation of the super large ring truss occur under the tension of the cable mesh, and the calculation accuracy is insufficient if the traditional method is used. Therefore, this paper proposes a cable mesh pretension method that considers the large deformation of the ring truss. According to the simulation test results, this method can ensure that the antenna mesh model has high accuracy and that the cable mesh pretension and the initial design pretension change very little after the whole ring antenna has stable cable mesh pretension. Therefore, it can be used to guide the design of the cable mesh pretension for the deployable ring antenna with a super large aperture.

Considering the discreteness of mechanical properties of different composite thin-walled pipe fittings, it is to achieve a more accurate design of cable mesh, the mechanical parameters of the bar can be tested and updated to the calculation program.

The mesh is usually not unloaded during the development of large ring deployable antenna. For the super large aperture ring deployable antenna, the weight of cable mesh will significantly impact the antenna surface accuracy and the mesh pretension distribution. According to the FDM, relevant modeling and simulation can be carried out in the ground gravity environment to guide the profile adjustment in the gravity environment to ensure that the antenna meets the surface accuracy and cable mesh tension requirements in orbit.

Data Availability

The data that support the findings of this study are available from the corresponding author with a reasonable request.

Conflicts of Interest

The authors declare that they have no conflicts of interest.

Acknowledgments

This work was supported by the National Natural Science Foundation of China (U1537213).

References

[1] M. W. Thomson, "The AstroMesh deployable reflector," in *IEEE Antennas and Propagation Society International Symposium. 1999 Digest. Held in conjunction with: USNC/URSI National Radio Science Meeting (Cat. No.99CH37010)*, pp. 1516–1519, Orlando, FL, USA, July 1999.

[2] F. Angeletti, P. Gasbarri, and M. Sabatini, "Optimal design and robust analysis of a net of active devices for micro- vibration control of an on-orbit large space antenna," *Acta Astronautica*, vol. 164, pp. 241–253, 2019.

[3] T. Li, J. Jiang, H. Deng, Z. Lin, and Z. Wang, "Form-finding methods for deployable mesh reflector antennas," *Chinese Journal of Aeronautics*, vol. 26, no. 5, pp. 1276–1282, 2013.

[4] L. Wang and L. Dong-Xu, "Simple technique for form-finding and tension determining of cable-network antenna reflectors," *Journal of Spacecraft and Rockets*, vol. 50, no. 2, pp. 479–481, 2013.

[5] S. Morterolle, B. Maurin, J. Quirant, and C. Dupuy, "Numerical form-finding of geotensoid tension truss for mesh reflector," *Acta Astronautica*, vol. 76, pp. 154–163, 2012.

[6] H.-J. Schek, "The force density method for form finding and computation of general networks," *Computer Methods in Applied Mechanics and Engineering*, vol. 3, no. 1, pp. 115–134, 1974.

[7] Z. Chu, Z. Deng, X. Qi, and B. Li, "Modeling and analysis of a large deployable antenna structure," *Acta Astronautica*, vol. 95, pp. 51–60, 2014.

[8] S. Pellegrino, "Analysis of prestressed mechanisms," *International Journal of Solids and Structures*, vol. 26, no. 12, pp. 1329–1350, 1990.

[9] S. Pellegrino, "Structural computations with the singular value decomposition of the equilibrium matrix," *International Journal of Solids and Structures*, vol. 30, no. 21, pp. 3025–3035, 1993.

[10] W. Liu, D. X. Li, X. Z. Yu, and J. P. Jiang, "Exact mesh shape design of large cable-network antenna reflectors with flexible ring truss supports," *Acta Mechanica Sinica*, vol. 30, no. 2, pp. 198–205, 2014.

[11] P. Yuan, B. He, L. Zhang, Z. Yuan, and X. Ma, "Pretension design of cable-network antennas considering the deformation of the supporting truss: a double-loop iterative approach," *Engineering Structures*, vol. 186, pp. 399–409, 2019.

[12] Y. Peng, Z. Zhao, M. Zhou, J. He, J. Yang, and Y. Xiao, "Flexible multibody model and the dynamics of the deployment of mesh antennas," *Journal of Guidance, Control, and Dynamics*, vol. 40, no. 6, pp. 1499–1510, 2017.

[13] K. Fu, Z. Zhao, G. Ren et al., "From multiscale modeling to design of synchronization mechanisms in mesh antennas," *Acta Astronautica*, vol. 159, pp. 156–165, 2019.

[14] Z. Zhao, K. Fu, M. Li, J. Li, and Y. Xiao, "Gravity compensation system of mesh antennas for in-orbit prediction of deployment dynamics," *Acta Astronautica*, vol. 167, pp. 1–13, 2020.

[15] M. A. XiaoFei, Y. A. JunGang, H. U. JianFeng, X. Zhang, X. I. Yong, and Z. H. ZhiHua, "Deployment dynamical numerical simulation on large elliptical truss antenna," *SCIENTIA SINICA Physica, Mechanica & Astronomica*, vol. 49, no. 2, article 024516, 2019.

[16] J. F. Hu, Y. Xiao, and Z. H. Zhao, "Dynamic simulation on the large sized hoop truss antenna during deploying," *Science Technology and Engineering*, vol. 12, no. 16, pp. 171–176, 2016.

[17] J. Hu, J. Yang, Y. Xiao et al., "Dynamic simulation of the deployment process of super large loop antenna belt," *Chinese Space Science and Technology*, vol. 41, no. 5, pp. 50–56, 2021.

[18] G. Tibert, *Numerical Analysis of Cable Roof Structures*, Royal Institute of Technology, Stockholm, 1999.

[19] G. Tibert, "Optimal design of tension truss antennas," in *44th AIAA/ASME/ASCE/AHS/ASC Structures, Structural Dynamics, and Materials Conference*, p. 1629, Norfolk, Virginia, April 2003.

[20] J. C. Simo and L. Vu-Quoc, "On the dynamics in space of rods undergoing large motions – a geometrically exact approach," *Computer Methods in Applied Mechanics and Engineering*, vol. 66, no. 2, pp. 125–161, 1988.

[21] J. C. Simo and L. Vu-Quoc, "A three-dimensional finite-strain rod model. Part II: computational aspects," *Computer Methods in Applied Mechanics and Engineering*, vol. 58, no. 1, pp. 79–116, 1986.

[22] A. A. Shabana, *Dynamics of Multibody Systems*, Cambridge University Press, 2009.

[23] M. A. Crisfield and G. Jelenić, "Geometrically exact 3D beam theory: implementation of a strain-invariant finite element for statics and dynamics," *Computer Methods in Applied Mechanics and Engineering*, vol. 171, no. 1-2, pp. 141–171, 1999.

[24] K. E. Dufva, J. T. Sopanen, and A. M. Mikkola, "A two-dimensional shear deformable beam element based on the absolute nodal coordinate formulation," *Journal of Sound and Vibration*, vol. 280, no. 3–5, pp. 719–738, 2005.

[25] Z. Zhao and G. Ren, "A quaternion-based formulation of Euler–Bernoulli beam without singularity," *Noliner Dynamics*, vol. 67, no. 3, pp. 1825–1835, 2012.

[26] Z. Dayu, L. Jianjun, W. Hui, and M. Xiaofei, "Locking problem and locking alleviation of ANCF/CRBF planar beam elements," *Chinese Journal of Theoretical and Applied Mechanics*, vol. 53, no. 3, pp. 874–889, 2021.